AGU100 ADVANCING EARTH AND SPACE SCIENCE

JGR

Journal of Geophysical Research: Space Physics

RESEARCH ARTICLE

10.1029/2018JA026037

Key Points:

- A first-principles description of the fast magnetosonic mode propagating at the dipole magnetic equator is provided
- A direct comparison between the simulated and observed wave polarization properties is made
- Wave amplification occurs dominantly during azimuthal propagation in the source region

Supporting Information:

- Supporting Information S1
- Movie S1
- Movie S2
- Movie S3

Correspondence to:
K. Min,
kyungguk@me.com

Citation:
Min, K., Boardsen, S. A., Denton, R. E., & Liu, K. (2018). Equatorial evolution of the fast magnetosonic mode in the source region: Observation-simulation comparison of the preferential propagation direction. *Journal of Geophysical Research: Space Physics*, *123*, 9532–9544. https://doi.org/10.1029/2018JA026037

Received 28 AUG 2018
Accepted 10 NOV 2018
Accepted article online 16 NOV 2018
Published online 28 NOV 2018

Equatorial Evolution of the Fast Magnetosonic Mode in the Source Region: Observation-Simulation Comparison of the Preferential Propagation Direction

Kyungguk Min[1,2], Scott A. Boardsen[3,4], Richard E. Denton[5], and Kaijun Liu[6]

[1]Space Science Institute, Boulder, CO, USA, [2]Korea Astronomy and Space Science Institute, Daejeon, South Korea, [3]Goddard Planetary Heliophysics Institute, University of Maryland, Baltimore, MD, USA, [4]NASA/GSFC, Greenbelt, MD, USA, [5]Department of Physics and Astronomy, Dartmouth College, Hanover, NH, USA, [6]Department of Physics, Auburn University, Auburn, AL, USA

Abstract Recent analysis of an event observed by the Van Allen Probes in the source region outside the plasmapause has shown that fast magnetosonic waves (also referred to as equatorial noise) propagate preferentially in the azimuthal direction, implying that wave amplification should occur during azimuthal propagation. To demonstrate this, we carry out 2-D particle-in-cell simulations of the fast magnetosonic mode at the dipole magnetic equator with the simulation box size, the magnetic field inhomogeneity, and the plasma parameters chosen from the same event recently analyzed. The self-consistently evolving electric and magnetic field fluctuations are characterized by spectral peaks at harmonics of the local proton cyclotron frequency. The azimuthal component of the electric field fluctuations is larger than the radial component, indicating wave propagation mainly along the azimuthal direction. Because the simulation box is within the source region, this also implies wave amplification mainly during azimuthal propagation. The excellent agreement between the wave polarization properties of the present simulations and the recently reported observations is clear evidence that the main wave amplification occurs during azimuthal propagation in the source region.

1. Introduction

Fast magnetosonic waves (also known as equatorial noise) are one of the frequently observed electromagnetic emissions in the inner magnetosphere (Boardsen et al., 2016; Hrbáčková et al., 2015; Ma et al., 2013; Meredith et al., 2008; Němec et al., 2005; Posch et al., 2015; Santolík et al., 2004; Tsurutani et al., 2014). They play an important role in the dynamics of energetic ring current ions and radiation belt electrons (Bortnik & Thorne, 2010; Chen et al., 2015; Horne et al., 2007; Li et al., 2015). The *fast magnetosonic* label originated from phenomenological observations in which the dispersion properties of the observed electric and magnetic field fluctuations were well described by the high-frequency (above the proton cyclotron frequency) extension of the fast magnetosonic branch, or the whistler branch, at propagation quasi-perpendicular to the background magnetic field, $\mathbf{B}_0$, in cold electron-proton plasmas (e.g., Boardsen et al., 1992; Laakso et al., 1990; Perraut et al., 1982). This means that for a single linear mode, the longitudinal component of the electric field fluctuations is much stronger than the transverse component and hence the major axis of the electric field polarization ellipsoid is closely aligned with the wave normal direction and the group velocity direction (e.g., Boardsen et al., 1992, 2016; Santolík et al., 2002).

Němec et al. (2013) used this fact to derive the preferential propagation direction of the fast magnetosonic mode observed in the inner magnetosphere. They analyzed 10 years of Cluster observations and showed statistically that azimuthal propagation is dominant where the (total) plasma number density is low ($n_0 \lesssim 30$ cm^{-3}), as occurs outside the plasmapause, but no preferential propagation direction is found where the density is high ($n_0 \gtrsim 100$ cm^{-3}), as occurs inside the plasmapause. Recently, Boardsen et al. (2018) analyzed the burst mode captures of the electric and magnetic field fluctuations for the event presented by Min, Liu, Wang, et al. (2018) to investigate the electric field polarization properties in a region corresponding to the low densities of Němec et al. (2013). They revealed that the propagation direction is not only dominantly in the azimuthal direction but also biased eastward. Since Min, Liu, Wang, et al. (2018) showed that the simultaneously observed partial shell velocity distribution of energetic protons was responsible for the observed wave excitation, the results of Boardsen et al. (2018) indicate that the wave amplification should preferentially occur during azimuthal propagation in the source region. The preferential azimuthal propagation can also be explained by trapping at the plasmapause density gradient (Chen & Thorne, 2012; Kasahara et al., 1994), but the observations were made far away from the plasmapause (Min, Liu, Wang, et al., 2018, Figure 2), thereby ruling out this possibility.

The only analysis of convective wave amplification of this mode (Horne et al., 2000; Shklyar & Balikhin, 2017) was restricted to the meridional plane, but the preferential amplification in the azimuthal direction may be theoretically understood (e.g., Boardsen et al., 2014, 2016) as follows: The wave normal angle of the fast magnetosonic mode is close to 90°, and in that situation, this mode becomes unstable only in the vicinity of the local proton cyclotron frequency (Chen, 2015; Gulelmi et al., 1975). Therefore, propagation in the azimuthal direction can keep the fast magnetosonic mode in resonance for a long distance (provided that the azimuthal extent of the source region is sufficiently large). Those satellite observations that often show electromagnetic fluctuations of this wave mode exhibiting spectral peaks at harmonics of the local proton cyclotron frequency (Balikhin et al., 2015; Min, Liu, Wang, et al., 2018) may be a strong support for this conjecture. The recent 1-D particle-in-cell (PIC) simulations of Min, Liu, Denton, et al. (2018) showed that the amplification of the fast magnetosonic mode propagating radially in the dipole magnetic field is very inefficient compared to the wave amplification in the uniform background magnetic field, favoring the preferential amplification during azimuthal propagation. On the other hand, an outward refraction of the magnetosonic mode in a nearly axis-symmetric medium (Chen & Thorne, 2012) may prevent waves from staying in this optimal path. Also recently, Chen et al. (2018) carried out first 2-D PIC simulations of the fast magnetosonic mode in a meridional plane with free energy localized near the center of the simulation domain. Unlike the results of Min, Liu, Denton, et al. (2018; where free energy was uniformly distributed), their results appear to show dominant radial propagation of the magnetosonic mode with very well organized electric and magnetic wavefields (most likely because the radial extent of the source region in Chen et al., 2018, was relatively small).

In support for the recent event study by Boardsen et al. (2018) and to provide an explanation for the statistical findings by Němec et al. (2013) in the low density regions, the present study will test the hypothesis that the azimuthal direction is the preferred direction for propagation and amplification of fast magnetosonic waves in the source region. We extend the PIC simulations of Min, Liu, Denton, et al. (2018) to 2-D geometry to provide a first-principles description of the fast magnetosonic mode for the same event recently analyzed and to demonstrate that the observed polarization properties presented in Boardsen et al. (2018) can be produced when considering wave measurements in the source region. Because the wave normal angles of the observed waves were shown to be close to 90° (Boardsen et al., 2018) and they were observed close to the magnetic equator (Min, Liu, Wang, et al., 2018), we consider spatial variations in the radial and azimuthal directions at the magnetic equator assuming a dipole background magnetic field.

The paper is organized as follows. Section 2 further details the present simulation setup, and section 3 describes the simulation results. In section 4, the simulated electric and magnetic field fluctuations are analyzed in the same way as Boardsen et al. (2018) for a direct comparison with the observed polarization properties. Section 5 summarizes the results.

2. Simulation Setup

As described in Min, Liu, Denton, et al. (2018), curvilinear coordinates (q^1, q^2, and q^3) for dipole geometry are q^1 varying along field lines, q^2 varying radially, and q^3 varying in the azimuthal direction. The present 2-D configuration on the dipole magnetic equator has $q^1 = 0$ and

$$\begin{aligned} q^2 &= \frac{r_{0,\mathrm{ref}}}{\Delta_2} \frac{r_0^3}{3r_{0,\mathrm{ref}}^3}, \\ q^3 &= \frac{r_{0,\mathrm{ref}}}{\Delta_3} \phi, \end{aligned} \tag{1}$$

where Δ_2 and Δ_3 are the scale lengths of the q^2 and q^3 coordinates, respectively, r_0 is the radial distance to a field line, ϕ is the azimuthal angle to that field line, and the subscript *ref* denotes values at some reference

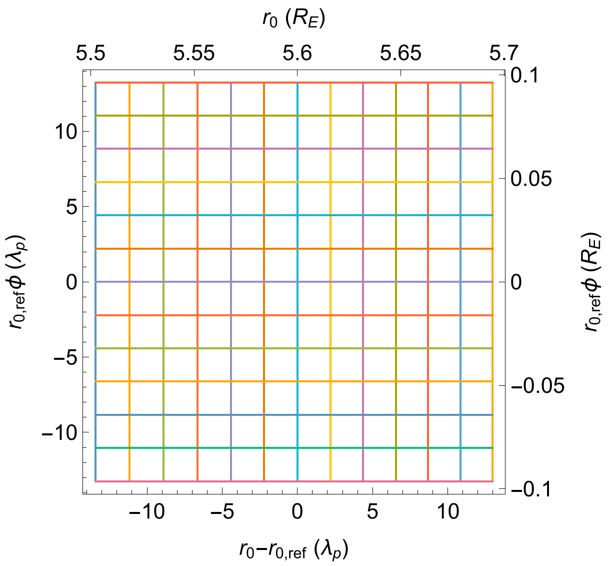

Figure 1. Equatorial simulation domain with reduced grid points in polar coordinates. The left and bottom axes are in units of the proton inertial length, λ_p, and the right and top axes are in units of the Earth radius, R_E. The azimuthal angle ϕ spans ±1°. The simulation domain size roughly corresponds to 16 wavelengths for the fourth harmonic.

field line (to be determined). As in Min, Liu, Denton, et al. (2018), the grid size in curvilinear space is uniform $\Delta q^2 \times \Delta q^3 = 1 \times 1$, corresponding approximately to $\Delta_2 \times \Delta_3$ in real space.

The simulation domain is centered at $r_0 = r_{0,\mathrm{ref}}$ and $\phi = 0$. The wave event presented by Min, Liu, Wang, et al. (2018) is used to select the necessary parameters. The observations (Min, Liu, Wang, et al., 2018, Figure 2) show strong wave activity occurring roughly within 0.2 R_E centered at a radial distance of about 5.6 R_E near the magnetic equator and roughly within 7.5° of the magnetic local time (about 0.73 R_E). Understanding that the hypothesis to be tested will favor a large azimuthal extent of the source region, we nevertheless choose the simulation box size of roughly 0.2×0.2 R_E centered at $r_{0,\mathrm{ref}} = 5.6$ R_E in the dipole magnetic field. Limited computational resources available were the main reason for this choice. But by providing an equal length to grow in both directions, this setup will tell us whether wave amplification indeed prefers one direction over the other when the given conditions are roughly the same. We will discuss the situation where the source region is elongated in the azimuthal direction in section 5.

Since the event occurred near the midnight sector, we will consider $\phi = 0°$ as midnight magnetic local time. Eastward and westward for the present study are the increasing and decreasing ϕ directions, respectively. It is preferable to normalize the length scales by the proton inertial length, the ratio of the light speed to the proton plasma frequency ($\lambda_p = c/\omega_{pp}$), because the wavelength of the fast magnetosonic mode is scaled by this characteristic length. Based on the observed total plasma number density of $n_0 = 24$ cm^{-3}, the proton inertial length is $\lambda_p \approx 0.00727$ R_E, and hence, $r_{0,\mathrm{ref}} = 770$ λ_p. If we choose $\Delta_2 = \Delta_3 = 0.05$ λ_p (same as in Min, Liu, Denton, et al., 2018), the number of grid points of 528×528 roughly corresponds to 0.2 R_E in both the radial and azimuthal directions. The simulation domain size is about 16 wavelengths for the fourth harmonic (whose wavelength is about 1.57 λ_p). The background magnetic field strength at the inner and outer boundaries in the radial direction is 1.054 $B_{0,\mathrm{ref}}$ and 0.951 $B_{0,\mathrm{ref}}$, respectively, where $B_{0,\mathrm{ref}}$ is the dipole magnetic field magnitude at $r_0 = r_{0,\mathrm{ref}}$. The simulation domain, but showing fewer grid points, is displayed in Figure 1.

For the initial plasma, we choose the same three-component plasma as in Min, Liu, Denton, et al. (2018). The first component is the partial shell velocity distribution of energetic protons that will excite the fast

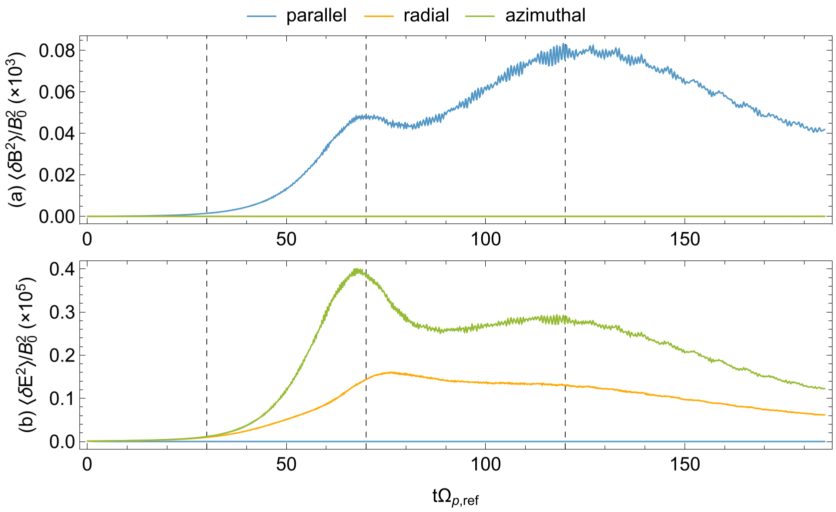

Figure 2. Time evolution of the fluctuating (a) magnetic and (b) electric field energy densities. The three colored lines denote the three components in field-aligned coordinates as labeled. The vertical lines are drawn at $t\Omega_{p,\mathrm{ref}} = 30$, 70, and 120, respectively.

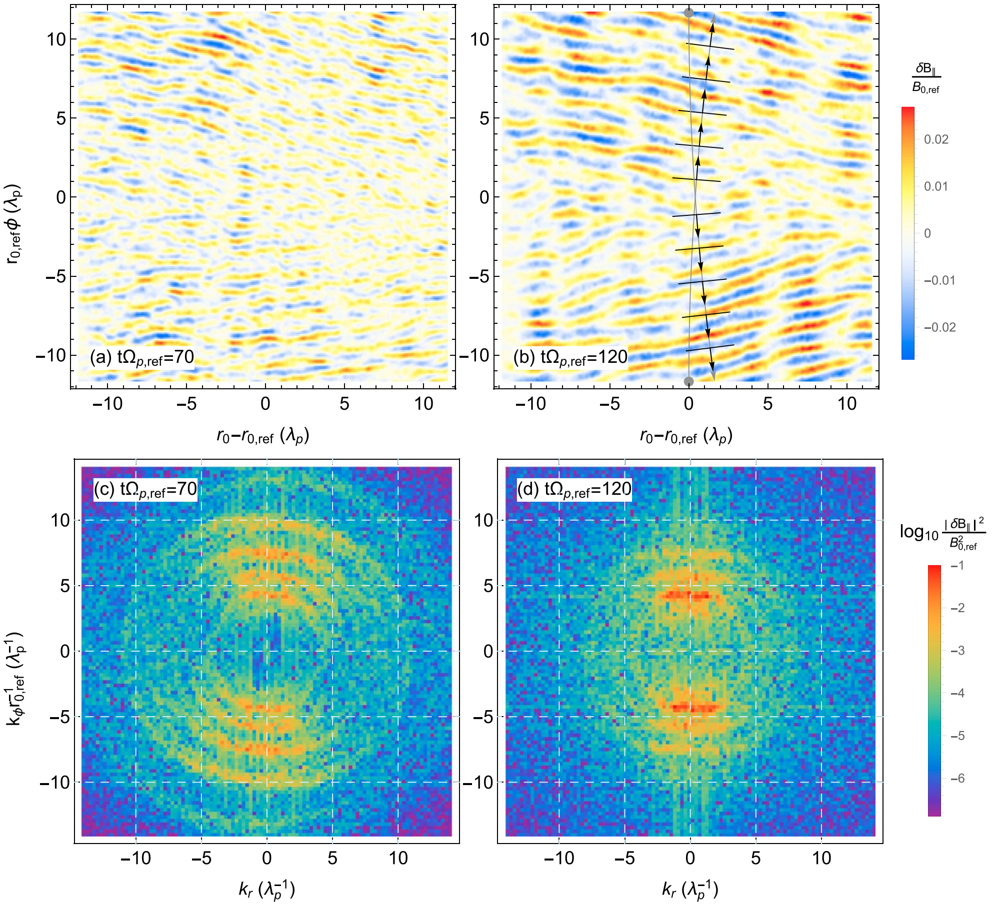

Figure 3. (a, b) Snapshots of the compressional component ($\delta B_\parallel$) of the fluctuating magnetic field at $t\Omega_{p,\mathrm{ref}} = 70$ and 120, respectively, shown in $r_0-\phi$ space (see Figure 1). The gray curves in panel b represent the paths of two rays with real frequency $\omega_r/\Omega_p = 4$ launched at the azimuthal boundaries (gray solid dots) and $r_0 = r_{0,\mathrm{ref}}$. The arrows indicate the wave normal directions at the locations of arrow tail for the later halves of the raypaths. (c, d) Corresponding wave number spectrograms of $\delta B_\parallel$. The fourth harmonic mode can be identified at $|k_\phi| r_{0,\mathrm{ref}}^{-1} \approx 4\lambda_p^{-1}$ and $k_r \sim 0$ in both panels and the seventh harmonic mode at $|k_\phi| r_{0,\mathrm{ref}}^{-1} \approx 10\lambda_p^{-1}$ and $k_r \sim 0$ in panel c.

magnetosonic mode self-consistently as shown in Min, Liu, Wang, et al. (2018)

$$f_s = \frac{n_s}{\pi^{3/2}\theta_s^3 C(v_s/\theta_s)} e^{-(v-v_s)^2/\theta_s^2} \sin^l \alpha, \tag{2}$$

where n_s is the number density, v_s is the shell speed, θ_s is the thermal spread of the shell, l is the pitch angle anisotropy index, and

$$C(b) = \left[b e^{-b^2} + \sqrt{\pi}\left(\frac{1}{2} + b^2\right) \mathrm{erfc}\,(-b)\right] \frac{\Gamma(1 + l/2)}{\Gamma(1.5 + l/2)}.$$

Here erfc (x) is the complementary error function and $\Gamma(x)$ is the gamma function. Note the following relation

$$\frac{T_{\perp s}}{T_{\parallel s}} = \frac{\int_0^\pi \sin^{3+l} \alpha d\alpha}{2\int_0^\pi \sin^{1+l} \alpha \cos^2 \alpha d\alpha} = \frac{2+l}{2},$$

where $T_{\perp s}$ and $T_{\parallel s}$ are the effective temperatures of the partial shell in directions perpendicular and parallel to the background magnetic field, respectively. Consistent with Min, Liu, Wang, et al. (2018), we choose $n_s = 0.05\ n_0$, $l = 1$, $v_s = 1.7\ v_{A,\mathrm{ref}}$, and $\theta_s = 0.43\ v_{A,\mathrm{ref}}$, where $v_{A,\mathrm{ref}} = B_{0,\mathrm{ref}}/\sqrt{4\pi m_p n_0}$ denotes the Alfvén speed at $r_0 = r_{0,\mathrm{ref}}$. The second component is a Maxwellian (obtained by setting $l = v_s = 0$) representing the remaining protons with the number density $n_b = n_0 - n_s$. As in Min, Liu, Denton, et al. (2018), we choose small but

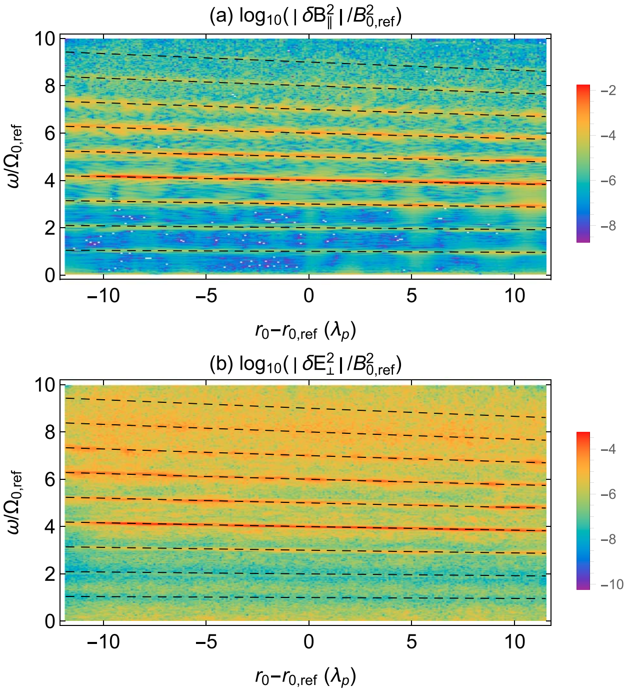

Figure 4. Power spectra of (a) the compressional component of the fluctuating magnetic field ($\delta B_\parallel$) and (b) the perpendicular component of the fluctuating electric field ($\delta E_\perp$) as a function of wave frequency and radial location. The entire time series sampled at $r_{0,\mathrm{ref}}\phi = -10\lambda_p$ are used to produce the figure. The wave frequency is normalized to $\Omega_{p,\mathrm{ref}}$, and the dashed horizontal curves are drawn at harmonics of the local proton cyclotron frequency from 1 to 9.

finite temperature so that the plasma beta of this population is $\beta_b = 8\pi n_b T_b/B_{0,\mathrm{ref}}^2 = 0.00475$, where T_b is the temperature of this population. The last component represents charge-neutralizing electrons with $\beta_e = 0.005$. This three-component plasma is uniformly distributed initially in the simulation domain; this can be justified from relatively small variation of the total density during the wave event (Min, Liu, Wang, et al., 2018, Figure 2e). Min, Liu, Wang, et al. (2018) showed that although the partial shell distribution is anisotropic ($T_{\perp s}/T_{\parallel s} = 1.5$), the growth of electromagnetic ion cyclotron waves at propagation parallel to the background magnetic field is negligible.

To facilitate the computations, we use a reduced ratio of the proton-to-electron mass, $m_p/m_e = 100$, and a reduced ratio of the light to Alfvén speed, $c/v_{A,\mathrm{ref}} = 30$. The integration time step is $\Delta t\Omega_{p,\mathrm{ref}} = 0.001$, where $\Omega_{p,\mathrm{ref}} = eB_{0,\mathrm{ref}}/m_p c$ is the angular proton cyclotron frequency at $r_0 = r_{0,\mathrm{ref}}$. The number of simulation particles per cell is 5,000 for the partial shell protons and 2,500 for the background protons and electrons, respectively. For waves, open boundary conditions are used in both directions using the masking method (Umeda et al., 2001); the number of wave masking grid points is 30 (corresponding roughly to one proton inertial length) at each boundary. For particles, periodic boundary conditions are used in the azimuthal direction and reflecting boundary conditions (Hu, 2010) are used in the radial direction.

The linear theory solutions corresponding to the initial setup are shown in Min, Liu, Denton, et al. (2018) and will not be repeated here. The results showed that the real part of the solutions closely follows the cold plasma extraordinary dispersion relation due to the low temperature of the background populations. In addition, harmonic modes from 3 to 9 are unstable at the center of the simulation domain, with the fourth harmonic being the fastest growing mode. (The harmonic is defined in terms of the local proton cyclotron frequency, $\Omega_p(r_0) = eB_0(r_0)/(m_p c)$, where $B_0(r_0)$ is the dipole magnetic field magnitude at r_0.) The lower hybrid frequencies, $\omega_{lh} = \Omega_p/\sqrt{v_A^2/c^2 + m_e/m_p}$ (v_A is the local Alfvén speed), at the inner radial boundary, at $r_0 = r_{0,\mathrm{ref}}$, and at the outer radial boundary are $\omega_{lh} = 9.43$, 9.49, and $9.53\Omega_p$ (or $\omega_{lh} = 9.95$, 9.49, and $9.07\Omega_{p,\mathrm{ref}}$), respectively.

The values of ω_{lh} for the present setup are significantly smaller than the real value of $\sim 42\ \Omega_p$. This results in fewer harmonic modes that can be excited (see, e.g., Min, Liu, Wang, et al., 2018, Figure 3). Several studies (Gao et al., 2017; Min & Liu, 2016; Min, Liu, Wang, et al., 2018) nevertheless provided some justifications that despite the reduced number of the harmonics, the fundamental physics of wave-particle interactions that drive the main dynamics can still be understood from scaled-down simulations such as those presented here. Chen et al. (2016), Sun, Gao, Chen, et al. (2016) and Sun, Gao, Lu, et al. (2016) cautioned, however, that the once discrete frequency spectrum of the excited waves can become continuous when the real value of m_p/m_e is used because of the increasing linear growth rate with the increasing m_p/m_e. This will not be a problem in the present study because the linear theory analysis in Min, Liu, Wang, et al. (2018; from which our initial particle distributions were derived) showed that the spectrum still remains discrete.

Recently, Chen et al. (2018) presented first 2-D PIC simulations of the magnetosonic mode in a meridional plane. It is worth comparing the differences and similarities in the initial setup between the present simulations and theirs. Obviously, the region of interest is different: We are concerned with the equatorial evolution of the magnetosonic mode, whereas they focused on the evolution along the field line and in the radial direction from a source confined in the radial direction and near the magnetic equator. The background magnetic field inhomogeneity also differs: The radial distance to the center of the simulation box in the present simulations coincides with where the event of Min, Liu, Wang, et al. (2018) occurred, whereas Chen et al. (2018) assumed a scaled-down system where the magnetic field inhomogeneity is 4–6 times larger than that of the realistic inner magnetosphere (the corresponding L shell is 1). Lastly, the initial energetic proton velocity distribution, the background plasma density, and the simulation box size in the present simulations are guided by the actual measurements, whereas in Chen et al. (2018), these parameters were chosen based on their earlier theoretical/modeling work (Chen et al., 2016; Sun, Gao, Chen, et al., 2016; Sun et al., 2017; Sun, Gao, Lu, et al., 2016). Note that the maximum linear growth rate is about 0.1 Ω_p for the present simulations and about 0.5 Ω_p for Chen et al. (2018). On the other hand, both simulations assumed reduced values for $c/v_{A,\mathrm{ref}}$ and m_p/m_e to reduce the computational costs.

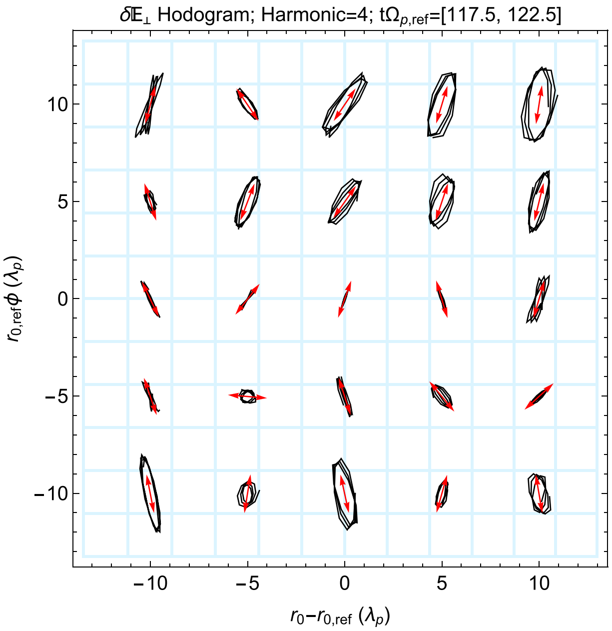

Figure 5. Hodograms of $\delta\mathbf{E}_\perp \equiv \delta E_r\mathbf{e}_r + \delta E_\phi\mathbf{e}_\phi$ corresponding to the fourth harmonic mode sampled at 5 × 5 uniformly spaced grid points between $t\Omega_{p,\mathrm{ref}} = 117.5$ and 122.5. The double-headed arrows indicate the major axis direction of the polarization ellipses obtained from the minimum variance method. The signals were band-pass filtered in frequency between $\omega_r = 3.5$ and $4.5\Omega_p$.

3. Simulation Results

We first describe the self-consistent evolution of the fast magnetosonic mode. Figure 2 shows the time evolution of the fluctuating magnetic and electric field energy densities. The evolution may be divided into three phases: (1) the exponential growth phase up to $t\Omega_{p,\mathrm{ref}} \approx 70$, (2) the saturation phase between $t\Omega_{p,\mathrm{ref}} \approx 70$ and 120, and (3) the decay phase afterward. The magnetic field energy is dominated by the compressional component ($\delta B_\parallel$; blue), and the electric field energy is dominated by the perpendicular component ($\delta\mathbf{E}_\perp \equiv \delta E_r\mathbf{e}_r + \delta E_\phi\mathbf{e}_\phi$; orange and green). The electric field energy clearly exhibits an inequality $|\delta E_\phi|^2 > |\delta E_r|^2$ for $t\Omega_{p,\mathrm{ref}} \gtrsim 30$, suggesting preferential wave propagation/amplification in the azimuthal direction. Even though the radial component of the electric field energy is smaller than the azimuthal component, both components have the same order of magnitude. As will be shown in the next paragraph, however, this does not mean that there is substantial amplification during radial propagation.

Figure 3 shows snapshots of the compressional component ($\delta B_\parallel$) of the fluctuating magnetic field at $t\Omega_{p,\mathrm{ref}} = 70$ and 120 and the corresponding wave number spectrograms. (See also movies in the supporting information.) Similar to the 1-D simulations of Min, Liu, Denton, et al. (2018), the waves start to grow near the inner radial boundary where the linear growth rate is slightly larger. Once $|\delta E_\phi| > |\delta E_r|$ after $t\Omega_{p,\mathrm{ref}} \approx 30$, a pattern of bidirectional wave propagation clearly emerges: One group of waves propagates toward the increasing ϕ direction (eastward) at the upper half plane ($\phi \gtrsim 0$), and another group propagates toward the decreasing ϕ direction (westward) at the lower half plane ($\phi \lesssim 0$). Note that the wave normal directions have a small radial component pointing outward regardless of the azimuthal propagation direction. This may be attributed to the refraction of the fast magnetosonic mode under the framework of geometric optics when propagating in the background magnetic field with a radial gradient (Chen & Thorne, 2012; Kasahara et al., 1994). To show this, two raypaths with real frequency $\omega_r/\Omega_p = 4$ (the strongest mode for the present case) launched at the azimuthal boundaries (gray dots) and $r_0 = r_{0,ref}$ are superimposed in Figure 3b. For ray tracing, we followed the standard ray tracing formulation assuming the cold plasma extraordinary mode dispersion relation (e.g., Shklyar & Balikhin, 2017). The arrows, which are placed at the second halves of the raypaths, indicate the wave normal directions at those locations. These are close to the direction of the group velocity (along the gray curves). Qualitative agreement of the wave normal directions from the simulation (perpendicular to the wavefronts) and the ray tracing supports the above conjecture, although it appears that the wavefronts from the simulation are slanted outward slightly more than the prediction from ray tracing. (Note that ray tracing considers a single mode, whereas the waves in the simulation are a superposition of many different modes.)

The wave number spectrograms in Figures 3c and 3d show several discrete spectral peaks along the k_ϕ axis near $k_r = 0$. In Figure 3c, these peaks correspond to the harmonic modes from 4 (at $|k_\phi|r_{0,\mathrm{ref}}^{-1} \approx 4\lambda_p^{-1}$) to 7 (at $|k_\phi|r_{0,ref}^{-1} \approx 10\lambda_p^{-1}$). In Figure 3d, the seventh harmonic mode has decayed away, while the third harmonic mode has grown out of the noise floor at $|k_\phi|r_{0,\mathrm{ref}}^{-1} \approx 3\lambda_p^{-1}$. Consistent with the simulations in a uniform background magnetic field of Min, Liu, Wang, et al. (2018), the higher harmonic modes tend to evolve faster than the lower harmonics, explaining the inverse cascade of power toward lower wave numbers as time progresses. The anisotropy of wave power in k_r–k_ϕ space is, again, evidence for the preferential wave

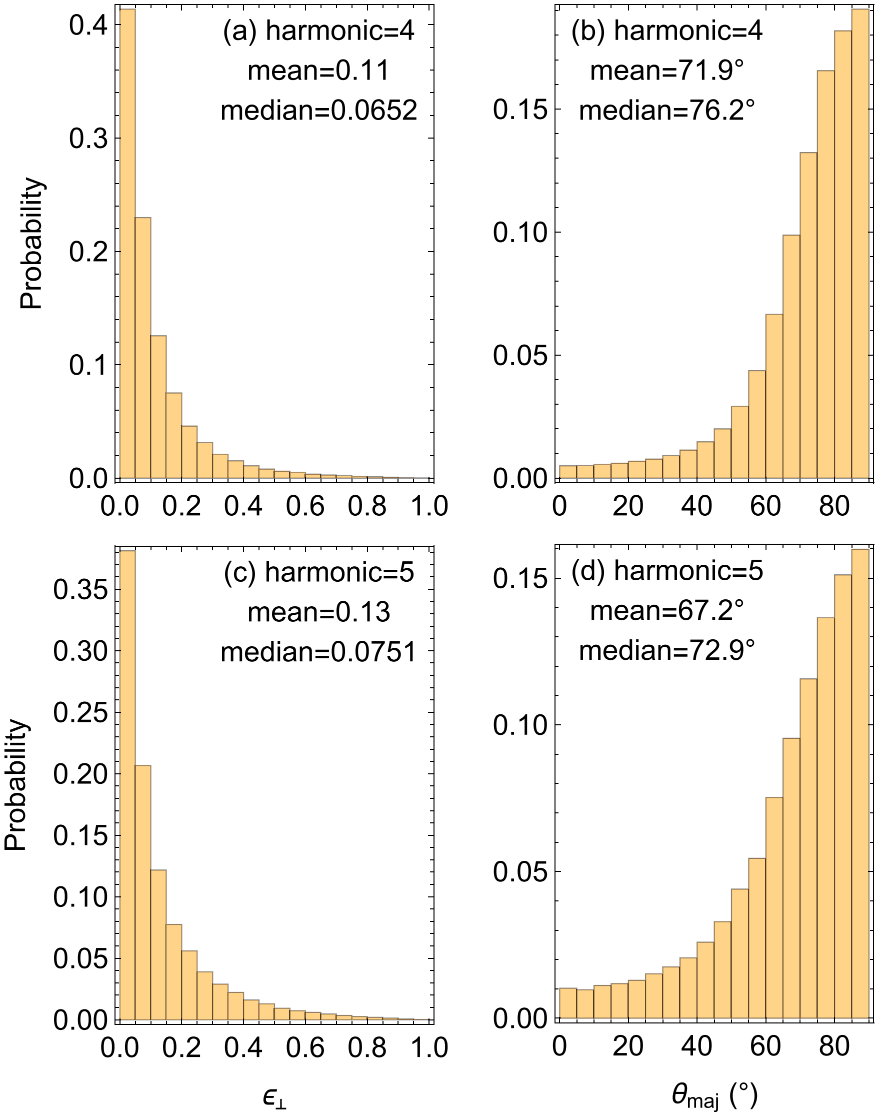

Figure 6. Results of minimum variance analysis on $\delta\mathbf{E}_\perp$. (a, c) Histograms of the ratio of the minimum to maximum variances ($\epsilon_\perp$). (b, d) Histograms of the angle (folded into the first quadrant) between the maximum variance direction and the radial vector ($\theta_{\rm maj}$). The mean and median values are labeled in each panel. The first and second rows are for the fourth and fifth harmonic modes, respectively. The time intervals of signals used are $t\Omega_{p,\rm ref} = [80, 150]$ for the fourth harmonic mode and $t\Omega_{p,\rm ref} = [70, 110]$ for the fifth harmonic mode.

propagation/amplification occurring in the azimuthal direction. We note that similarities can be found between Figures 3c and 3d and Kasahara et al. (1994, Figures 10 and 13) where these authors applied the wave distribution function analysis on the satellite measurements of the three-component magnetic field. (They only resolved wave normal directions, not the magnitude.)

Figure 4 shows the wave power of $\delta B_\parallel$ and $\delta\mathbf{E}_\perp$ as a function of frequency and radial distance, produced using the entire time series sampled at $r_{0,\rm ref}\phi = -10\lambda_p$ (Figure 1). Note that the wave frequency is normalized to $\Omega_{p,\rm ref}$. First, the spectra exhibit narrow spectral peaks, and second, the frequencies at which these peaks occur closely follow the harmonics of the local proton cyclotron frequency indicated by the dashed horizontal curves. By comparing with Boardsen et al. (2018, Figure 1), these features are in excellent agreement with those from the Van Allen Probes observations. This provides strong support for the conclusion of Boardsen et al. (2018) that wave amplification mainly occurred in the azimuthal direction for the event considered. (Otherwise, the harmonic spectral structure should have been washed out as shown in Min, Liu, Denton, et al., (2018, Figure 8b). On the other hand, the simulation shows far less harmonic modes because of the reduced m_p/m_e used.

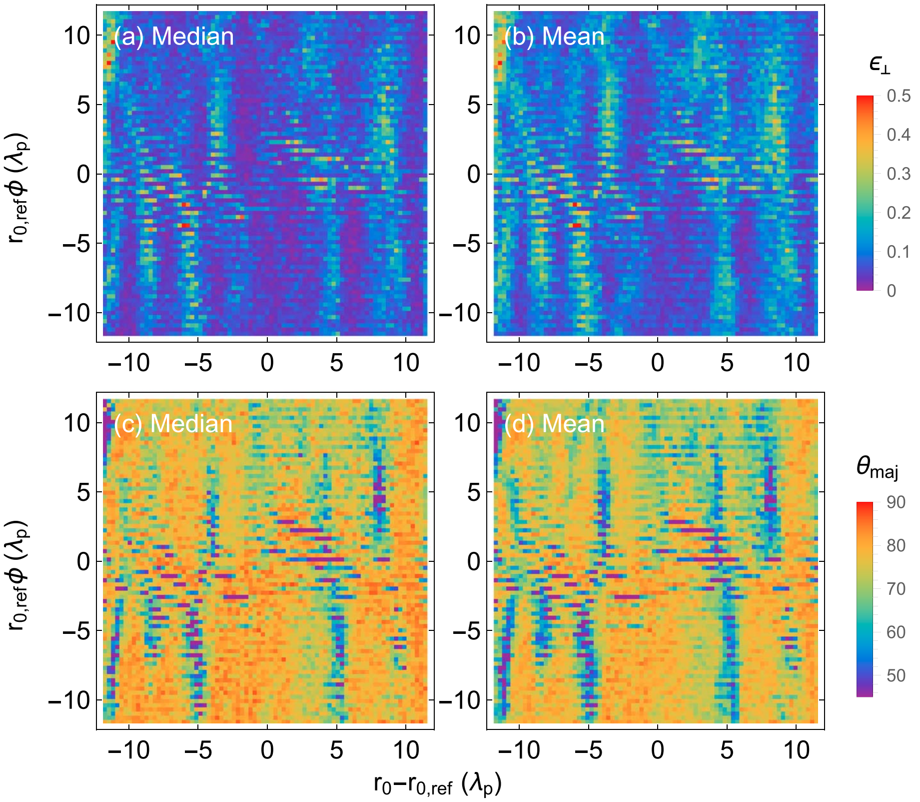

Figure 7. Spatial dependence of (a, b) the mean and median of the ratio of the minimum to maximum variances ($\epsilon_\perp$) and (c, d) the angle (folded into the first quadrant) between the maximum variance direction and the radial vector (θ_{maj}) corresponding to the fourth harmonic mode. Panels a and c show the median values, and panels b and d show the mean values of the corresponding quantities. These statistics were derived from about 22 samples in each pixel. The time intervals of signals used are $t\Omega_{p,\mathrm{ref}} = [80, 150]$.

4. Polarization Analysis

In this section, we analyze the fluctuating electric and magnetic fields in detail and compare the simulated wave polarization properties with those from the observations presented in Boardsen et al. (2018). Figure 5 shows hodograms of $\delta\mathbf{E}_\perp$ corresponding to the fourth harmonic mode sampled at 5×5 uniformly spaced grid points between $t\Omega_{p,\mathrm{ref}} = 117.5$ and 122.5. The signals were band-pass filtered in frequency between $\omega_r = 3.5$ and $4.5\Omega_p$. Although there is a small amount of variation, in general, $\delta\mathbf{E}_\perp$ is elliptically polarized and the major axis directions of the polarization ellipses are roughly along the azimuthal direction. These hodograms are consistent with the example shown by Němec et al. (2013, Figure 3) from Cluster.

For a more quantitative comparison with the results of Boardsen et al. (2018), we carried out minimum variance analysis on the simulated $\delta\mathbf{E}_\perp$. For a given harmonic mode and at a given grid point, the time series of signals were divided into four wave cycles moving in steps of two wave cycles. The individual four cycle-long signals were fed into the minimum variance method (e.g., Means, 1972) to calculate the ratio of the minimum to maximum variances ($\epsilon_\perp$) of the polarization ellipse and the angle (folded into the first quadrant) between the maximum variance direction and the radial vector (θ_{maj}), resulting in an array of pairs ($\epsilon_\perp, \theta_{\mathrm{maj}}$) at every grid point. (This is equivalent to the wavestep analysis of Anderson et al., 1996, and Min et al., 2017.) We selected the samples at 78×78 uniformly spaced grid points, resulting in $78\times78\times N_t$ samples of ($\epsilon_\perp, \theta_{\mathrm{maj}}$) to work with, where N_t is the number of samples in the time dimension which varies depending on the harmonic mode.

Figure 6 shows histograms of $\epsilon_\perp$ and θ_{maj} corresponding to the fourth and fifth harmonic modes. The time intervals of signals used are $t\Omega_{p,\mathrm{ref}} = [80, 150]$ for the fourth harmonic mode and $t\Omega_{p,ref} = [70, 110]$ for the fifth harmonic mode. These time intervals produce histograms most consistent with those from the observations. The reason for different time intervals can be understood from the differing time scale of evolution

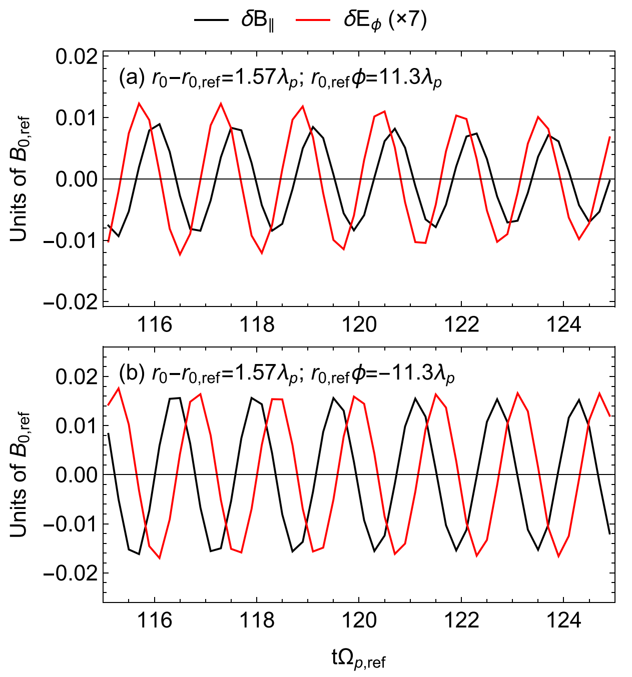

Figure 8. Time series of $\delta B_\parallel$ (black) and δE_ϕ (red; scaled up by a factor of 7) sampled at $r_0 - r_{0,\mathrm{ref}} = 1.57\lambda_p$ and (a) $r_{0,\mathrm{ref}}\phi = 11.3\lambda_p$ or (b) $r_{0,\mathrm{ref}}\phi = -11.3\lambda_p$. The signals were band-pass filtered in frequency between $\omega_r = 3.5$ and 4.5 Ω_p.

depending on the harmonic number, but the overall trend is the same even if different time intervals were chosen. As anticipated from Figure 5, $\delta\mathbf{E}_\perp$ is dominantly elliptically polarized ($\epsilon_\perp \sim 0$) with the major axis of the polarization ellipses oriented in the azimuthal direction ($\theta_{\mathrm{maj}} \sim 90°$). These histograms are nearly identical to Boardsen et al. (2018, Figures 4d and 4e) constructed from the Van Allen Probe burst captures. The major difference is the more elevated level of the θ_{maj} histograms near 0°. The likely reason is the low saturation amplitudes of the magnetosonic mode relative to the noise level. On the one hand, the shorter azimuthal extent of the source region limits convective wave growth, and on the other hand, the noise level in the simulation is inherently large because the number of simulation particles is still far less than the actual number of particles in the inner magnetosphere. (Support for this explanation is given in the supporting information.) Another possibility may be the difference between the wavestep analysis of the present study and the Fourier analysis of Boardsen et al. (2018). We examined the sixth harmonic mode also; other than larger spread of histograms due perhaps to the weaker wave power, the same trend was found.

Figure 7 presents the spatial distributions of mean and median values of the $\epsilon_\perp$ and θ_{maj} samples corresponding to the fourth harmonic mode at 78×78 grid points. There are about 22 samples in each bin. (The same data set was used to draw Figures 6a and 6b.) As noticed from Figures 6a and 6b, there are relatively large variations which appear to correspond to the irregular pattern of the wavefield in Figures 3a and 3b. But in a larger scale, the distributions are roughly uniform in a sense that there is no large-scale asymmetry.

Boardsen et al. (2018) showed that the phase difference between δE_L (the longitudinal component of the electric field fluctuations) and $\delta B_\parallel$ can be used to determine the sign in Figures 6b and 6d. Linear theory in the cold plasma regime shows that $\delta E_L/\delta B_\parallel = i(D/S)/(k_\perp/\omega_r)$ for the fast magnetosonic mode at 90° wave normal angle (Boardsen et al., 2018), where D and S are the Stix parameters (Stix, 1992). In the fast magnetosonic frequency range, $\Omega_p < \omega_r < \omega_{lh}$, the imaginary part of $\delta E_L/\delta B_\parallel$ is negative for a forward propagating mode ($\omega_r > 0$ and $k_\perp > 0$). Because the wave normal directions are approximately along the azimuthal direction for the present simulation (Figure 3), δE_ϕ may be regarded as δE_L. (We also used the wave normal directions from the two rays shown in Figure 3b to derive δE_L and got essentially the same results.) Figure 8a shows the time series of $\delta B_\parallel$ and δE_ϕ sampled at $r_0 - r_{0,\mathrm{ref}} = 1.57\lambda_p$ and $r_{0,\mathrm{ref}}\phi = 11.3\lambda_p$ (near the end of the ray propagating eastward in Figure 3b). The signals were band-pass filtered in frequency between $\omega_r = 3.5$ and $4.5\Omega_p$. The δE_ϕ signal is lagging behind $\delta B_\parallel$ by about 90°. This is as though a virtual satellite sees the wave propagating dominantly eastward out of the simulation domain. Similarly, Figure 8b shows the time series of the two signals sampled at $r_0 - r_{0,\mathrm{ref}} = 1.57\lambda_p$ and $r_{0,\mathrm{ref}}\phi = -11.3\lambda_p$ (near the end of the ray propagating westward in Figure 3b). Now the phase difference is flipped. This is as though a virtual satellite sees the wave propagating dominantly westward out of the simulation domain. These results are consistent with the prediction of linear theory for waves propagating eastward (Figure 8a) or westward (Figure 8b).

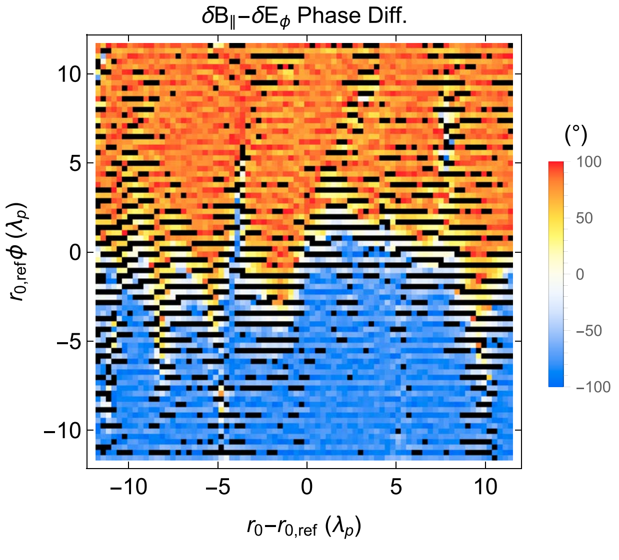

Figure 9. Spatial map of the phase difference between $\delta B_\parallel$ and δE_ϕ at $t\Omega_{p,\mathrm{ref}} = 120$ corresponding to the fourth harmonic mode. Positive (reddish color) means eastward propagation. The black pixels are where the phase angle is beyond the range of [−100, 100]°.

Figure 9 shows the spatial distribution of the phase difference between $\delta B_\parallel$ and δE_ϕ corresponding to the fourth harmonic mode. The four cycle-long signals centered at $t\Omega_{p,\mathrm{ref}} = 120$ were used for the phase calculation. The phase difference is close to 90° near the eastward boundary and −90° near the westward boundary, consistent with the picture from the single-point evaluation (Figure 8). That the phase angles are grouped in the vicinity of 90° in Boardsen et al. (2018, Figure 4f) indicates that the spacecraft was located eastward of the source region when the event occurred. The transition near $\phi = 0°$ is more of a step-like function than a smooth transition. Therefore, it is more likely that spacecraft measurements will show grouping in the vicinity of either −90° or 90°.

5. Conclusions and Discussions

Recent analysis of an event observed by the Van Allen Probes (Boardsen et al., 2018) has shown that fast magnetosonic waves propagate preferentially in the azimuthal direction near or in the source region, implying that the main wave amplification should occur during azimuthal propagation. To confirm this, we carried out a 2-D PIC simulation of the fast magnetosonic mode in dipole geometry. Given that the wave normal angles were close to 90° for the event (Boardsen et al., 2018) and that the waves were detected close to the magnetic equator, we chose spatial variation at the dipole magnetic equator, thereby simulating equatorial evolution of the fast magnetosonic mode. The simulation box size, the magnetic field inhomogeneity, and the initial plasma parameters were chosen from the same event recently analyzed.

The waves that self-consistently evolved in the simulation were characterized by spectral peaks at harmonics of the local proton cyclotron frequency with the electric field fluctuations dominantly in the azimuthal direction. The simulated waves were analyzed in a way similar to that of Boardsen et al. (2018) for a direct comparison of the wave polarization properties reported there. The excellent agreement between the observed and simulated electric field polarization properties was clear evidence that the wave amplification for the observed fast magnetosonic mode occurred during azimuthal propagation in the source region.

Although the observations showed that the azimuthal extent of the source region was more than 3 times larger, we chose a simulation box with equal sides, understanding that this setup is more stringent for convective wave amplification in the azimuthal direction. To examine the effect of a larger azimuthal extent of the source region, we carried out a simulation where the simulation box size in the azimuthal direction was increased by a factor of 3. To reduce computation time, however, we decreased the number of simulation particles by a factor of 10 and treated background protons and electrons as cold, linearized fluids (Tao, 2014). (So only the partial shell protons were discrete particles.) Understandably, wave amplitudes in this simulation are larger both because of a larger spatial length for magnetosonic waves to grow and because there was no damping by thermal populations. But still, the waves excited exhibit propagation dominantly in the azimuthal direction followed by an outward refraction. In addition, the electric field polarization properties and the bimodal structure of the $\delta B_{\parallel} - \delta E_{\phi}$ phase difference are consistent with those from the present simulation with equal sides. This indicates that the present conclusions still hold even for a source region whose azimuthal extent is larger than the radial extent and that the azimuthal direction is indeed the direction favored for wave amplification for the event of Boardsen et al. (2018). One feature less clear in the present simulation with equal sides is that the waves propagate both eastward and westward near the center meridian of the source region, where the phase difference tends to 0 (or otherwise not well defined). (See the supporting information for detailed analysis.)

The present simulation results are in support for the initial conjecture that for a dipole background magnetic field and when the plasma density is only a function of the radial distance, the waves will experience growth over a much longer raypath for waves propagating in the azimuthal direction as opposed to the radial direction, if launched at the magnetic equator with a normal angle of 90°. The statistical findings of the azimuthal propagation angle distribution in the low density regions shown by Němec et al. (2013) may be interpreted in this context, understanding that the plasma trough is often considered to be the source region (e.g., Horne et al., 2000; Ma, Li, Chen, Thorne, Angelopoulos, et al., 2014). According to the simple gain analysis of Boardsen et al. (2018) using a dipole magnetic field model with constant density and the growth rate formula and ring distribution of Chen (2015), the path integrated gain over 0.5 R_E for a magnetosonic wave propagating in the azimuthal direction is 5 times larger than the gain of a wave propagating in the radial direction; the wave propagating radially goes out of resonance after propagating only 0.1 R_E. It appears that their analysis could have been easily generalized, perhaps in a way similar to Shklyar and Balikhin (2017), to reveal the preferential propagation direction.

Although there is still a lot of room for ray tracing with the path integrated gain analysis, kinetic simulations can offer at the expense of the longer computational time a detailed wave structure (which allowed us to perform spectral and phase analyses to make a direct comparison with the observations) and the evolution of the plasma species (which Min, Liu, Wang, et al., 2018, used to make a direct comparison with the observations).

For the magnetosonic mode, mode conversion as a wave propagates across $n\Omega_p$ (n being an integer) can be a potential problem in ray tracing. One typically uses the cold plasma approximation for the real part of the dispersion relation and the warm plasma to compute the gain. Boardsen et al. (1992) and Horne et al. (2000) used the mode conversion formula given by Ngan and Swanson (1977) to argue that as a wave approaches $n\Omega_p$ for a 90° wave normal angle, the transmission coefficient is ~ 1, and only a small amount of energy is reflected or ends up on the ion Bernstein mode branch. The driven simulations in Min, Liu, Denton, et al. (2018) also supports this.

One of the hypotheses for explaining the magnetosonic wave population observed inside the plasmapause is propagation inward from outside source regions (e.g., Ma, Li, Chen, Thorne, Kletzing, et al., 2014; Němec et al., 2013; Su et al., 2017). According to Chen & Thorne (2012; and also as suggested by various other studies), if a wave generated outside the plasmasphere has a substantial component of the wave normal vector pointing radially toward the Earth, it can potentially propagate a long distance across the plasmapause and in the azimuthal direction. The dominant waves in the present simulation, however, have a small radial component of the wave normal vector away from the Earth. This is in fact consistent with the statistical results of Němec et al. (2013) who noticed that waves in low density regions tend to have a small radial component of the wave normal vector away from the Earth. So after leaving the source region, these waves will continuously be refracted outward (Chen & Thorne, 2012) and eventually be absorbed by plasma sheet populations (Horne et al., 2000), thereby leaving little chance for them to contribute to the wave population in the plasmasphere.

Can the waves of smaller amplitudes leaving the inner radial boundary in the simulation contribute to the wave population inside plasmapause? Or more generally, under what condition(s) can radial propagation be dominant? Both Chen et al. (2018) and Min, Liu, Denton, et al. (2018) showed that waves can still be amplified while propagating radially if azimuthal propagation is suppressed. This readily suggests that the radial versus azimuthal spatial scale of the source region is one factor that can determine the preferential wave propagation direction. However, the present simulation results as well as the gain analysis of Boardsen et al. (2018) indicate that the azimuthal extent of the source region need to be much smaller than the radial extent to allow (relatively) stronger convective wave growth in the radial direction. To confirm this, we carried out two more simulations with the azimuthal extent of the simulation box set to be half and a quarter of the radial extent, respectively. The waves grow more strongly at azimuthal propagation even if the azimuthal source extent is half the radial extent (not shown). When the azimuthal dimension is further reduced, the waves propagating radially can eventually dominate in the system. But since waves propagating radially go out of resonance quickly, their amplitude, if detected inside the plasmapause, will be generally low as suggested by Min, Liu, Denton, et al. (2018). Indeed, statistical magnetosonic wave distributions observed tend to show weaker power inside the plasmasphere (Boardsen et al., 2016; Kim & Chen, 2016; Ma et al., 2013; Meredith et al., 2008; Němec et al., 2015). The wavelength scale relative to the inhomogeneity scale may be another factor that affects the preferential wave propagation direction. If the wavelength is much smaller than the inhomogeneity scale, the background magnetic field may be considered to be uniform for wave's perspective. This situation can occur for high harmonic modes and/or in high density regions (where the characteristic wave scale is reduced). Last but not the least, the plasmapause density structure and nonuniform density profile in the azimuthal direction (like the plasmaspheric plume) can affect the preferential propagation direction through refraction (Chen & Thorne, 2012). (We have been assuming an axis-symmetric medium throughout the paper.)

Our model is by no means perfect; several assumptions were made in order to facilitate numerical calculations with limited computational resources. One such assumption is propagation exactly perpendicular to the background magnetic field. This assumption is well justified for the present study but may not be valid for all cases. Tsurutani et al. (2014) showed wave occurrence at high latitude, and Zhima et al. (2015) suggested that observations of discrete magnetosonic waves off the magnetic equator can be explained by a combination of parallel and radial propagation. Another issue is that the initial state of our simulation is not in MHD equilibrium. As a result, large-scale, quasi-steady perturbations arise, because the dipole magnetic field alone cannot counteract the particle pressure. The large-scale perturbations were indeed seen in the early phase of the present simulation. However, these perturbations are much weaker than the magnetosonic mode excited by the partial shell velocity distribution of energetic protons. Because the main dynamics are still governed by the magnetosonic mode and the associated wave-particle interactions, we anticipate that simulations with an initial MHD equilibrium would result in essentially the same conclusions of the present study. Finally, the use of reduced values for the light speed and the ratio of the proton-to-electron mass allowed fewer harmonic modes than what the observation showed. This was a necessary choice in order to reduce the simulation costs, and several studies (Gao et al., 2017; Min & Liu, 2016; Min, Liu, Wang, et al., 2018) provided some justifications that the fundamental physics of wave dynamics remains the same with these reduced parameters. On the other hand, studies also suggested that the exact spectral power and nonlinear dynamics may vary (Gao et al., 2017; Sun, Gao, Chen, et al., 2016; Sun, Gao, Lu, et al., 2016).

Acknowledgments
This work was completed in part with resources provided by the Auburn University Hopper Cluster. This research was supported by NASA grants NNX16AM98G and NNX17AI52G and NSF grants AGS-1602388 and AGS-1602469. Data sets used to produce figures are available in a Zenodo data repository at https://doi.org/10.5281/zenodo.1320491.

References

Anderson, B. J., Denton, R. E., & Fuselier, S. A. (1996). On determining polarization characteristics of ion cyclotron wave magnetic field fluctuations. *Journal of Geophysical Research*, *101*, 13,195–13,214. https://doi.org/10.1029/96JA00633

Balikhin, M. A., Shprits, Y. Y., Walker, S. N., Chen, L., Cornilleau-Wehrlin, N., Dandouras, I., et al. (2015). Observations of discrete harmonics emerging from equatorial noise. *Nature Communications*, *6*, 7703. https://doi.org/10.1038/ncomms8703

Boardsen, S. A., Gallagher, D. L., Gurnett, D. A., Peterson, W. K., & Green, J. L. (1992). Funnel-shaped, low-frequency equatorial waves. *Journal of Geophysical Research*, *97*, 14,967–14,976. https://doi.org/10.1029/92JA00827

Boardsen, S. A., Hospodarsky, G. B., Kletzing, C. A., Engebretson, M. J., Pfaff, R. F., Wygant, J. R., et al. (2016). Survey of the frequency dependent latitudinal distribution of the fast magnetosonic wave mode from Van Allen Probes electric and magnetic field instrument and integrated science waveform receiver plasma wave analysis. *Journal of Geophysical Research: Space Physics*, *121*, 2902–2921. https://doi.org/10.1002/2015JA021844

Boardsen, S. A., Hospodarsky, G. B., Kletzing, C. A., Pfaff, R. F., Kurth, W. S., Wygant, J. R., & MacDonald, E. A. (2014). Van Allen Probe observations of periodic rising frequencies of the fast magnetosonic mode. *Geophysical Research Letters*, *41*, 8161–8168. https://doi.org/10.1002/2014GL062020

Boardsen, S. A., Hospodarsky, G. B., Min, K., Averkamp, T. F., Bounds, S. R., Kletzing, C. A., & Pfaff, R. F. (2018). Determining the wave vector direction of equatorial fast magnetosonic waves. *Geophysical Research Letters*, *45*, 7951–7959. https://doi.org/10.1029/2018GL078695

Bortnik, J., & Thorne, R. M. (2010). Transit time scattering of energetic electrons due to equatorially confined magnetosonic waves. *Journal of Geophysical Research*, *115*, A07213. https://doi.org/10.1029/2010JA015283

Chen, L. (2015). Wave normal angle and frequency characteristics of magnetosonic wave linear instability,. *Geophysical Research Letters*, *42*, 4709–4715. https://doi.org/10.1002/2015GL064237

Chen, L., Maldonado, A., Bortnik, J., Thorne, R. M., Li, J., Dai, L., & Zhan, X. (2015). Nonlinear bounce resonances between magnetosonic waves and equatorially mirroring electrons. *Journal of Geophysical Research: Space Physics*, *120*, 6514–6527. https://doi.org/10.1002/2015JA021174

Chen, L., Sun, J., Lu, Q., Gao, X., Xia, Z., & Zhima, Z. (2016). Generation of magnetosonic waves over a continuous spectrum. *Journal of Geophysical Research: Space Physics*, *121*, 1137–1147. https://doi.org/10.1002/2015JA022089

Chen, L., Sun, J., Lu, Q., Wang, X., Gao, X., Wang, D., & Wang, S. (2018). Two-dimensional particle-in-cell simulation of magnetosonic wave excitation in a dipole magnetic field. *Geophysical Research Letters*, *45*, 8712–8720. https://doi.org/10.1029/2018GL079067

Chen, L., & Thorne, R. M. (2012). Perpendicular propagation of magnetosonic waves,. *Geophysical Research Letters*, *39*, L14102. https://doi.org/10.1029/2012GL052485

Gao, X., Liu, K., Wang, X., Min, K., Lin, Y., & Wang, X. (2017). Gyrokinetic electron and fully kinetic ion simulations of fast magnetosonic waves in the magnetosphere. *Physics of Plasmas*, *24*(6), 062901. https://doi.org/10.1063/1.4985303

Gulelmi, A. V., Klaine, B. I., & Potapov, A. S. (1975). Excitation of magnetosonic waves with discrete spectrum in the equatorial vicinity of the plasmapause. *Planetary and Space Science*, *23*, 279–286. https://doi.org/10.1016/0032-0633(75)90133-6

Horne, R. B., Thorne, R. M., Glauert, S. A., Meredith, N. P., Pokhotelov, D., & Santolík, O. (2007). Electron acceleration in the Van Allen radiation belts by fast magnetosonic waves. *Geophysical Research Letters*, *34*, L17107. https://doi.org/10.1029/2007GL030267

Horne, R. B., Wheeler, G. V., & Alleyne, H. S. C. K. (2000). Proton and electron heating by radially propagating fast magnetosonic waves. *Journal of Geophysical Research*, *105*, 27,597–27,610. https://doi.org/10.1029/2000JA000018

Hrbáčková, Z., Santolík, O., Němec, F., Macúšová, E., & Cornilleau-Wehrlin, N. (2015). Systematic analysis of occurrence of equatorial noise emissions using 10 years of data from the Cluster mission. *Journal of Geophysical Research: Space Physics*, *120*, 1007–1021. https://doi.org/10.1002/2014JA020268

Hu, Y. (2010). Hybrid code simulation of electromagnetic ion cyclotron waves in curvilinear coordinates (Ph.D. thesis), Dartmouth College.

Kasahara, Y., Kenmochi, H., & Kimura, I. (1994). Propagation characteristics of the ELF emissions observed by the satellite Akebono in the magnetic equatorial region. *Radio Science*, *29*, 751–767. https://doi.org/10.1029/94RS00445

Kim, K.-C., & Chen, L. (2016). Modeling the storm time behavior of the magnetosonic waves using solar wind parameters. *Journal of Geophysical Research: Space Physics*, *121*, 446–458. https://doi.org/10.1002/2015JA021716

Laakso, H., Junginger, H., Schmidt, R., Roux, A., & de Villedary, C. (1990). Magnetosonic waves above fc(H+) at geostationary orbit—GEOS 2 results. *Journal of Geophysical Research*, *95*, 10,609–10,621. https://doi.org/10.1029/JA095iA07p10609

Li, X., Tao, X., Lu, Q., & Dai, L. (2015). Bounce resonance diffusion coefficients for spatially confined waves,. *Geophysical Research Letters*, *42*, 9591–9599. https://doi.org/10.1002/2015GL066324

Ma, Q., Li, W., Chen, L., Thorne, R. M., & Angelopoulos, V. (2014). Magnetosonic wave excitation by ion ring distributions in the Earth's inner magnetosphere. *Journal of Geophysical Research: Space Physics*, *119*, 844–852. https://doi.org/10.1002/2013JA019591

Ma, Q., Li, W., Chen, L., Thorne, R. M., Kletzing, C. A., Kurth, W. S., et al. (2014). The trapping of equatorial magnetosonic waves in the Earth's outer plasmasphere. *Geophysical Research Letters*, *41*, 6307–6313. https://doi.org/10.1002/2014GL061414

Ma, Q., Li, W., Thorne, R. M., & Angelopoulos, V. (2013). Global distribution of equatorial magnetosonic waves observed by THEMIS. *Geophysical Research Letters*, *40*, 1895–1901. https://doi.org/10.1002/grl.50434

Means, J. D. (1972). Use of the three-dimensional covariance matrix in analyzing the polarization properties of plane waves. *Journal of Geophysical Research*, *77*, 5551–5559. https://doi.org/10.1029/JA077i028p05551

Meredith, N. P., Horne, R. B., & Anderson, R. R. (2008). Survey of magnetosonic waves and proton ring distributions in the Earth's inner magnetosphere. *Journal of Geophysical Research*, *113*, A06213. https://doi.org/10.1029/2007JA012975

Min, K., Denton, R. E., Liu, K., Gary, S. P., & Spence, H. E. (2017). Ion Bernstein instability as a possible source for oxygen ion cyclotron harmonic waves. *Journal of Geophysical Research: Space Physics*, *122*, 5449–5465. https://doi.org/10.1002/2017JA023979

Min, K., & Liu, K. (2016). Ion Bernstein instability dependence on the proton-to-electron mass ratio: Linear dispersion theory. *Journal of Geophysical Research: Space Physics*, *121*, 6692–6710. https://doi.org/10.1002/2016JA022850

Min, K., Liu, K., Denton, R. E., & Boardsen, S. A. (2018). Particle-in-cell simulations of the fast magnetosonic mode in a dipole magnetic field: 1D along the radial direction. *Journal of Geophysical Research: Space Physics*, *123*, 7424–7440. https://doi.org/10.1029/2018JA025666

Min, K., Liu, K., Wang, X., Chen, L., & Denton, R. E. (2018). Fast magnetosonic waves observed by Van Allen Probes: Testing local wave excitation mechanism. *Journal of Geophysical Research: Space Physics*, *123*, 497–512. https://doi.org/10.1002/2017JA024867

Němec, F., Santolík, O., Gereová, K., Macúšová, E., de Conchy, Y., & Cornilleau-Wehrlin, N. (2005). Initial results of a survey of equatorial noise emissions observed by the Cluster spacecraft. *Planetary and Space Science*, *53*, 291–298. https://doi.org/10.1016/j.pss.2004.09.055

Němec, F., Santolík, O., Hrbáčková, Z., & Cornilleau-Wehrlin, N. (2015). Intensities and spatiotemporal variability of equatorial noise emissions observed by the Cluster spacecraft. *Journal of Geophysical Research: Space Physics*, *120*, 1620–1632. https://doi.org/10.1002/2014JA020814

Němec, F., Santolík, O., Pickett, J. S., Hrbáčková, Z., & Cornilleau-Wehrlin, N. (2013). Azimuthal directions of equatorial noise propagation determined using 10 years of data from the Cluster spacecraft. *Journal of Geophysical Research: Space Physics*, *118*, 7160–7169. https://doi.org/10.1002/2013JA019373

Ngan, Y. C., & Swanson, D. G. (1977). Mode conversion and tunneling in an inhomogeneous plasma. *Physics of Fluids*, *20*, 1920–1937. https://doi.org/10.1063/1.861812

Perraut, S., Roux, A., Robert, P., Gendrin, R., Sauvaud, J.-A., Bosqued, J.-M., et al. (1982). A systematic study of ULF waves above F/H plus/from GEOS 1 and 2 measurements and their relationships with proton ring distributions. *Journal of Geophysical Research*, *87*, 6219–6236. https://doi.org/10.1029/JA087iA08p06219

Posch, J. L., Engebretson, M. J., Olson, C. N., Thaller, S. A., Breneman, A. W., Wygant, J. R., et al. (2015). Low-harmonic magnetosonic waves observed by the Van Allen Probes. *Journal of Geophysical Research: Space Physics*, *120*, 6230–6257. https://doi.org/10.1002/2015JA021179

Santolík, O., Nemec, F., Gereová, K., Macúšová, E., Conchy, Y., & Cornilleau-Wehrlin, N. (2004). Systematic analysis of equatorial noise below the lower hybrid frequency. *Annales Geophysicae*, *22*, 2587–2595. https://doi.org/10.5194/angeo-22-2587-2004

Santolík, O., Pickett, J. S., Gurnett, D. A., Maksimovic, M., & Cornilleau-Wehrlin, N. (2002). Spatiotemporal variability and propagation of equatorial noise observed by Cluster. *Journal of Geophysical Research*, *107*, 1495. https://doi.org/10.1029/2001JA009159

Shklyar, D. R., & Balikhin, M. A. (2017). Whistler mode waves below lower hybrid resonance frequency: Generation and spectral features. *Journal of Geophysical Research: Space Physics*, *122*, 10,072–10,083. https://doi.org/10.1002/2017JA024416

Stix, T. H. (1992). *Waves in plasmas*. New York: Am. Inst. of Phys.

Su, Z., Wang, G., Liu, N., Zheng, H., Wang, Y., & Wang, S. (2017). Direct observation of generation and propagation of magnetosonic waves following substorm injection. *Geophysical Research Letters*, *44*, 7587–7597. https://doi.org/10.1002/2017GL074362

Sun, J., Gao, X., Chen, L., Lu, Q., Tao, X., & Wang, S. (2016). A parametric study for the generation of ion Bernstein modes from a discrete spectrum to a continuous one in the inner magnetosphere. I. Linear theory. *Physics of Plasmas*, *23*(2), 022901. https://doi.org/10.1063/1.4941283

Sun, J., Gao, X., Lu, Q., Chen, L., Liu, X., Wang, X., et al. (2017). Spectral properties and associated plasma energization by magnetosonic waves in the Earth's magnetosphere: Particle-in-cell simulations. *Journal of Geophysical Research: Space Physics*, *122*, 5377–5390. https://doi.org/10.1002/2017JA024027

Sun, J., Gao, X., Lu, Q., Chen, L., Tao, X., & Wang, S. (2016). A parametric study for the generation of ion Bernstein modes from a discrete spectrum to a continuous one in the inner magnetosphere. II. Particle-in-cell simulations. *Physics of Plasmas*, *23*(2), 022902. https://doi.org/10.1063/1.4941284

Tao, X. (2014). A numerical study of chorus generation and the related variation of wave intensity using the DAWN code. *Journal of Geophysical Research: Space Physics*, *119*, 3362–3372. https://doi.org/10.1002/2014JA019820

Tsurutani, B. T., Falkowski, B. J., Pickett, J. S., Verkhoglyadova, O. P., Santolik, O., & Lakhina, G. S. (2014). Extremely intense ELF magnetosonic waves: A survey of polar observations. *Journal of Geophysical Research: Space Physics*, *119*, 964–977. https://doi.org/10.1002/2013JA019284

Umeda, T., Omura, Y., & Matsumoto, H. (2001). An improved masking method for absorbing boundaries in electromagnetic particle simulations. *Computer Physics Communications*, *137*, 286–299. https://doi.org/10.1016/S0010-4655(01)00182-5

Zhima, Z., Chen, L., Fu, H., Cao, J., Horne, R. B., & Reeves, G. (2015). Observations of discrete magnetosonic waves off the magnetic equator,. *Geophysical Research Letters*, *42*, 9694–9701. https://doi.org/10.1002/2015GL066255